Observability of Light Curve Shape Inversion Based on Optical Data

Alex Friedman,[(1)] **Siwei Fan,**[(1)]**, Carolin Frueh**[(1)] **and Thomas Schildknecht,**[(2)]

[(1)]School of Aeronautics & Astronautics, Purdue University, 701 W. Stadium Ave., West Lafayette, Indiana 47907 USA, friedmaa@purdue.edu, fan11@purdue.edu, cfrueh@purdue.edu
[(2)]Astronomical Institute, University of Bern, Sidlerstrasse 5, 3012 Bern, Switzerland, thomas.schildknecht@aiub.unibe.ch

ABSTRACT

The shape and attitude of resident space objects directly affect the orbit propagation via drag and solar radiation pressure. Obtaining information beyond an object state also is integral to identifying an object, aid in tracing its origin and its capabilities. For objects that have a significant distance to the observer, only non-resolved imaging is available, which does not reveal any details of the object. So-called non-resolved light curve measurements, i.e., brightness measurements over time, can be used to determine the shape of convex space objects using an inversion scheme. The inversion process starts by first determining the Extended Gaussian Image (EGI) and then solving the Minkowski problem to obtain the closed shape result. However, the light curve inversion problem is, by its nature, an under-determined problem. Hence, it is very sensitive to the sequencing of the observations collected. In this paper, the observability assessment for the light curve shape inversion problem is developed. The methodology is then applied to the observation sequencing of the Atlas V upper stage observed by the Astronomical Institute of the University of Bern (AIUB) Zimlat telescope. It is shown how observability conditions change based on telescope constraints and desired shape resolution.

1. INTRODUCTION

Identification of resident space object (RSO) characteristics beyond position and velocity can significantly impact the accuracy of orbit propagation due to drag and solar radiation pressure perturbation dependence on the shape and material properties. However, optical measurements of RSOs are often non-resolved, not revealing any details about the object because the distance between the observer and RSO is large. However, light curve inversion techniques aim to extract RSO characterization information from brightness measurements over time, otherwise known as light curves [1–7]. The inversion problem remains under-determined in its very nature. A light curve inversion technique for reliable inversion of convex objects in the presence of significant measurement noise has been developed by Fan and Frueh [1]. It relies on a variant of the process initially established by Kaasaleinen et al. [2]. These inversion techniques rely on being able to be performed in the object's body frame. Further details on the light curve inversion process, its constraints, and limitations can be found in [1]. Attitude determination in the absence of shape information is a complex topic to be solved without constraints. For time-stable, convex single-axis spinners, easy to implement methods exist even in the absence of shape information (beyond the convexity constraint) [8–12].

As shown in [13], the inversion problem, even its restricted form, is very sensitive to the input light curves data distribution. Inversion of unobservable cases cannot guarantee good inversion results and leading easily to detrimental distortion on the output shape, having little in common with the true shape. The relation of observability and estimatability for the orbit case has been illustrated in [14]. A workaround for light curve inversion has often been to demand absurdly large amounts of data for the inversion, something often not feasible even within night time constraints of an optical sensor and certainly not sustainable for characterization observation collection in a routine manner. Telescope operators, on the other hand, often adopted a more or less random approach to collecting shorter light curves to fit their operational constraints and balance observation time demands.

In order to find more efficient ways of collecting sufficient information for a shape inversion, an observability analysis for the light curve inversion problem has been developed. Observability, as a concept, explores the relationship between the measurements and states of a system. Observability has first been developed in the context of control theory [15–19] and has been applied to the RSO problem previously, focusing on the aspect of the orbital or orbital-attitude observability [20–29]. In this paper, the observability for the light curve inversion problem is investigated under the observation constraints of a real sensor.

Furthermore, the additional constraint that only short observation batches of the light curve measurements can be made. The batch lengths shown in this paper are 20 minutes each. In the presentation for this paper, the results for 10-minute batches are shown. In this paper, we focus on the application of the methodology to the Atlas V upper stage 14086B with real light curve measurement collected by the ZIMLAT telescope, located in Zimmerwald, Switzerland, which is owned and operated by the Astronomical Institute of the University of Bern. A more comprehensive treatment of the observability problem for shape inversion can be found in [13, 30].

2. METHODS

The light curve inversion process used as a baseline in this paper is depicted in Fig. 1, [1]. First, an Extended Gaussian Image (EGI) [31] is estimated in a constrained least-squares approach; subsequently, the Minkowski problem is solved in order to obtain adjacency information [32–34] via determination of each facet's support. The estimation of the EGI needs to be performed in the object's body frame. The support, the distance of each facet to the center of the object,

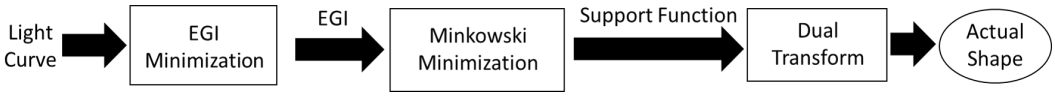

Fig. 1. Light curve inversion process .

is unobservable for observer distances ¿¿ than the support itself, which is the case in non-resolved observations. It is performed purely based on geometric principles. The light curve measurements are only used in the first step, the EGI estimation. In this paper, we focus hence, on the observability of the EGI determination process only.

2.1 EGI Mapping

An EGI is a projection of an arbitrary shape onto the surface of a unit sphere. Deviating from the classical definition [31], the surface areas are replaced via the albedo-area for the use in light curve measurements. For the discrete EGI representation adopted in this paper, the quad-cube projection is used, with a tessellation number of $m^2 \times 6$ for m being the number of facets per row and column on each side of the quad-cube projection. Examples of the EGI representation method are given in Fig. 2. The original object shapes are given in the first column of Fig. 2. The second column of

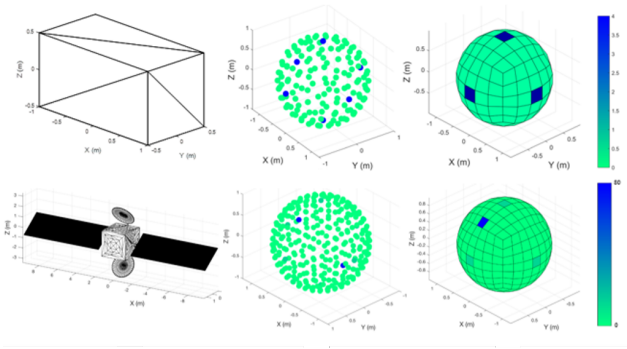

Fig. 2. Shape representation with an EGI [1] leading to a tesselation of 150 facets for the cuboid and 294 for the Astra satellite.

images in Fig. 2 show the dot representation of the EGI corresponding to each original object. The final column of images give the facet representation of the EGI for each original shape.

2.2 Observability

Observability of the light curve inversion problem begins with analysis of the optimization problem for determining the EGI:

$$J = |\boldsymbol{L} - G\,\boldsymbol{a}|^2, \tag{1}$$

where $\boldsymbol{L}$ is a vector of light curve measurements and $\boldsymbol{a}$ contains the albedo-area for each of the facets of the convex polygon, the quantity that is desired to be esimated. G is the reflection model matrix, determining the contribution

from each EGI normal direction under under a know light source strength and direction and observer geometry. Note that each of the variables above are time varying, i.e. $\boldsymbol{L} = \boldsymbol{L}(t),\ \boldsymbol{a} = \boldsymbol{a}(t),\ G = G(t)$. While solving this optimization problem, common observability analysis matrix forms do appear. Methods for deriving the least squares solution are implemented to come up with an 'observability Gramian' for this problem. Expanding the terms in Eq. 1 and simplifying,

$$= \boldsymbol{L}^T\ \boldsymbol{L} - 2\boldsymbol{a}^T\ G^T\ \boldsymbol{L} + \boldsymbol{a}^T\ G^T\ G\ \boldsymbol{a} \tag{2}$$

To find the least squares solution, $\hat{\boldsymbol{a}}$, the first derivative of J with respect to $\boldsymbol{a}$ is set equal to zero.

$$\frac{\partial J}{\partial \boldsymbol{a}} = \frac{\partial}{\partial \boldsymbol{a}}[\boldsymbol{L}^T\ \boldsymbol{L} - 2\boldsymbol{a}^T\ G^T\ \boldsymbol{L} + \boldsymbol{a}^T\ G^T\ G\ \boldsymbol{a}] = 0 \tag{3}$$

Finally, solving for $\hat{\boldsymbol{a}}$.

$$\hat{\boldsymbol{a}} = (G^T\ G)^{-1}\ G^T\ \boldsymbol{L} \tag{4}$$

The final step of solving for the optimum albedo-area for each of the surface normal directions relies on the assumption that $G^T\ G$ is non-singular. This is a fundamental component of testing the observability of a system. If the matrix can be inverted, then the system is said to be observable. For this problem, the observability relates to the ability to generate the albedo-areas of the EGI given the geometric setup of the problem in G. Note that the optimization is constrained to be positive as there cannot be negative albedo-areas.

3. RESULTS

The object of interest is the Atlas V upper stage with international designator 14068B. An approximated object is shown in Fig. 3 with three different types of surface materials, denoted by the colors white, black and yellow, based on known object specifications. Shape models are used for validation purposes.

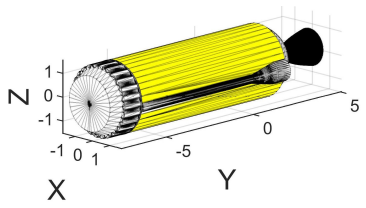

Fig. 3. Three material upper stage model for validation.

3.1 Attitude Profile

Under the assumption of a stable main-axis spinning motion, which is not unreasonable for large upper stages without significant slush fuel, the attitude has been determined. A likely attitude is determined using the methodology of Williams et al. [9] under the knowledge of a known phase angle using three light curves. The methodology relies on the coupling of the ratio of maximum brightness and minimum brightness with the spin axis. Using a single light curve, the locus of potential right ascension and declination angles of the spin axis can be formed. The attitude can be concluded from the intersection of two loci. The spin rate can be determined via Fourier analysis or periodogram methods.

Using the observational data of the night of May 9 2015 at 22:13 UTC over approximately 18 minutes, May 10 2015 from 22:51 UTC for approximately 14 minutes, May 14, 2:32 UTC lastin about 3 minutes. Koller determined the attitude profile of 14068B [35], with a the inertially fixed spin axis with a right ascension of 298° and declination of 9°as the mean of the overlap of the three loci, and a period of 64.7 s.

In order to validate the results, a brute-force search method to determine the spin axis directly by simulating the light curve using a full and a cylindrical simplified shape model and comparing it to the light curve measurements assuming the rotation period is exact. The spin axis was sampled at 1° resolution for both right ascension and declination for the May 10 light curve. Attitude A is defined by right ascension and declination of 318° and 9°, respectively. Attitude B is defined by right ascension and declination of 318° and 298°, respectively. Profile A provides a slightly better fit, hence, in the remainder of this work uses the attitude profile defined by Attitude A. Figure 4 shows the light curves

generated using the full object model (Fig. 3), a two-material cylinder shape and a uniform cylinder shape model and the observation data of May 10. It can be seen that the full model fits the observed light curve in orientation A the best in terms of the features, but that there is an albedo offset, which can be traced back to aging. The two-material cylinder, in orientation A and B fit the light curve well when the material properties are adapted, but it is missing out on some of the more delicate features due to the simplified shape.

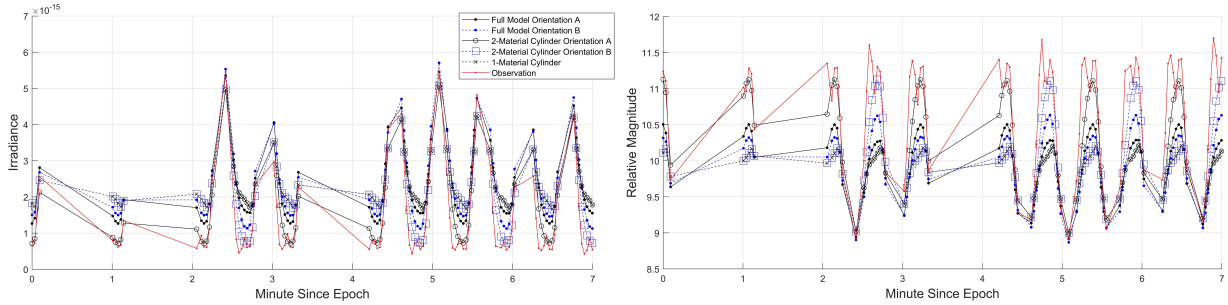

Fig. 4. Light curve comparison using different orientations of the spin axis and shape models.

3.2 Observability

Although the collected light curves provide sufficient measurements to find a good fitting attitude (albeit brute force sampling also found a second slightly better fitting one), the collected light curves do not allow for a shape inversion. Using the sensor location of the ZIMLAT sensor, the observation data of 14068B are approximated by a 20 minute batch of measurements with measurement spacing of two seconds, resulting in 600 measurements within each batch. The two second spacing is consistent with the CCD subframe technique used at the ZIMLAT telescope. A higher sampling rate, for example, achievable with AIUB's CMOS sensor, has been tested and did not provide advantages in terms of observability for the given slow-changing attitude profile. For illustration purposes, constraint-free observability results are shown and contrasted with the observability results enforcing a minimum elevation of 15 degrees and nighttime observation constraints, allowing only for observations between astronomical dusk and dawn.

Three EGI tessellations were used in this analysis with $m = 5, 7$, and 13, leading to tesselations 150, 294, and 1014 surface normal directions on the EGI, respectively. The half-angle between two neighboring angles is 3.6 deg, 2.7 deg, and 1.5 deg for tesselation of 150, 294, and 1014, respectively. In the subsequent figures, the rank of the EGI Gramian over time and the EGI Gramian as a function of the number of measurements are shown, respectively. In addition, the rank plots are zoomed in to show more detail near the full rank line, i.e., the number of surface normal directions on each EGI, given by the black dashed line.

3.2.1 Tesselation 150

Figure 5 shows the rank results for an EGI tessellation of 150 surface normal directions on the EGI. When the rank of the EGI Gramian reaches 150, the problem is considered full rank, and the number and spacing of measurements are sufficient for inverting the EGI Gramian to solve for the albedo-area vector. For this epoch and system, a significant amount of time is required until a sufficiently diverse geometry is offered to the observer to reach a full rank EGI Gramian. A rank of 146 is reached within the first batch of measurements already, as seen in Fig. 5b and Fig. 5d, but then the EGI Gramian does not become full rank until approximately 5 hours into the analysis time. Therefore, from the end of the first batch of measurements until approximately 5 hours from the start of the analysis, the geometry of the problem has not progressed enough for new measurements to increase the rank of the EGI Gramian. Additional measurements collected during this time period do not provide additional observability, and the sensor can focus on different tasks. Furthermore, Fig. 5b and Fig. 5d can be used to generate a more efficient strategy for obtaining light curve observations to be used in a light curve inversion process. In Fig. 5d, the 6 and 8 hour batch spacing cases both require the same number of batches, two, to reach full rank because the second batch for each case occurs after the 5 hour required time for the geometry of the problem to progress enough. Therefore, the 6 or 8 hour batch spacing cases may be selected for obtaining observations over the 4 hour case because fewer observations are required while reaching full rank of the EGI Gramian in the same amount of time or less. Hence, much flexibility is offered to adjust the sensor schedule balancing the light curve measurements with other observation tasks.

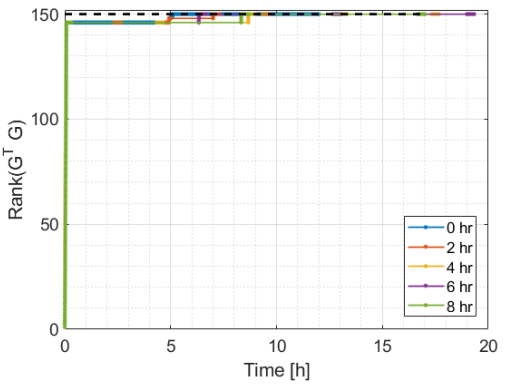

(a) Rank v. time

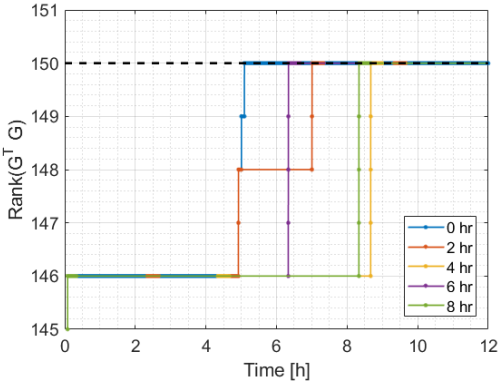

(b) Rank v. time, zoomed in to show detail

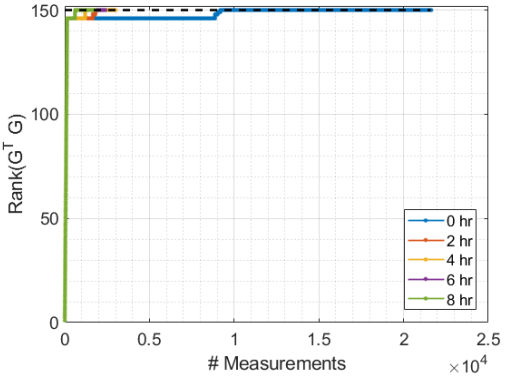

(c) Rank v. number of measurements

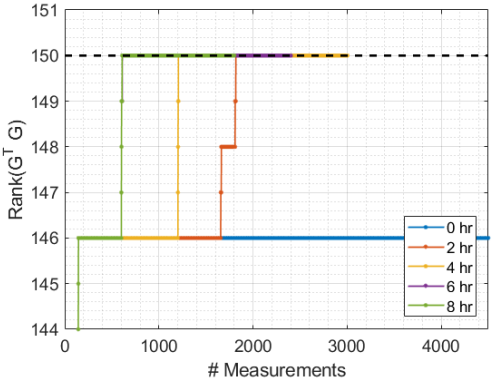

(d) Rank v. number of measurements, zoomed in to show detail

Fig. 5. Rank of the EGI Gramian for EGI tessellation of 150 facets.

3.2.2 Tesselation 294

Similar results for the rank of the EGI Gramian are shown in Fig. 6 with an EGI tessellation of 294 surface normal directions. For the 6 and 8 hour batch spacing cases, the time to reach full rank is longer than the same batch spacing cases of the smaller tesselation of 150. When the EGI tessellation is 158, the number of batches required is 2, but, not surprisingly, for the EGI tessellation 294, the number of batches required is 3 for the 6 and 8 hour batch spacing cases. Figure 6b shows how the 6 and 8 hour batch spacing cases reach a rank of 293 on the second batch of measurements, but require a third batch of measurements to reach full rank of 294. However, the 0, 2, and 4 hour batch spacing cases reached full rank in less than half the time of the 6 and 8 hour batch spacing cases. Therefore, the observability analysis exactly quantifies the trade-offs that can be made between higher resolution on the EGI and the available sensor observation time slots and limitations. It also shows that depending on the observation spacing, a higher tesselation is possible with the same number of measurements and time constraints.

For an EGI tessellation of 294, the 4 hour batch spacing case may be more advantageous than the 6 and 8 hour batch spacing cases because the time required for the EGI to reach full rank is shorter while the number of required measurement batches is equal.

3.2.3 Tesselation 294

For a good resolution with an angle error of 1.5 degrees only, a tesselation of 1014 ($m = 13$) surface normal vectors is desirable, being able to capture all of the bigger and medium sized features. For comparison, the simple cylindrical upper stage shape model for validation has a tesselation of 150 normal vectors, the full model shown in Fig.3, 4912 normal vectors.

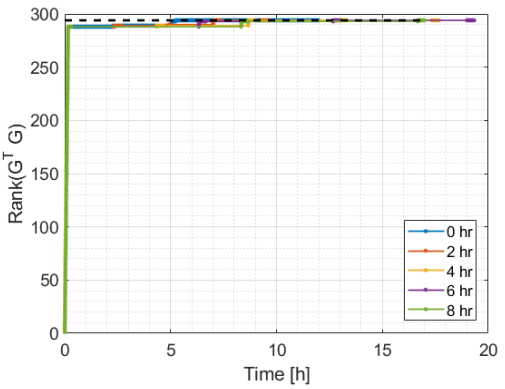

(a) Rank v. time

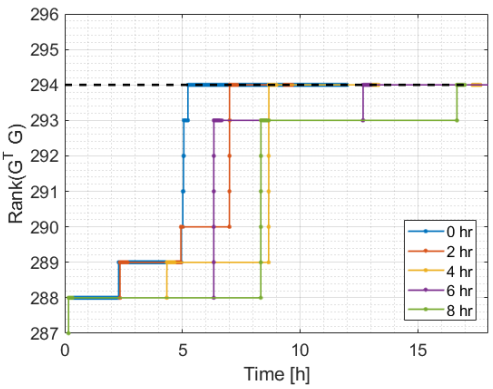

(b) Rank v. time, zoomed in to show detail

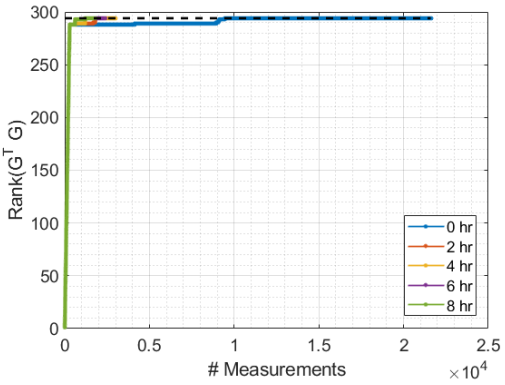

(c) Rank v. number of measurements

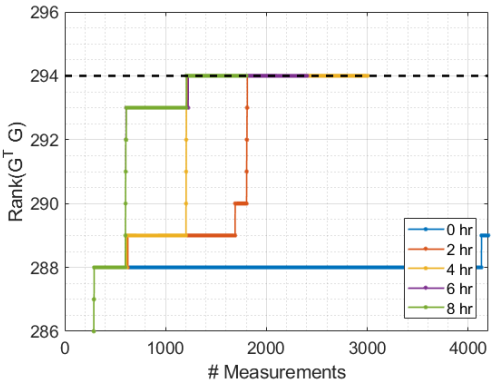

(d) Rank v. number of measurements, zoomed in to show detail

Fig. 6. Rank of the EGI Gramian for EGI tessellation of 294 facets.

In Fig. 7, the rank reaches 1013 for all of the batch spacing cases analyzed, but then there is a significant time required before the rank reaches 1014. The 2, 4, 6, and 8 hour batch spacing cases reach full rank in Fig. 7b, but the 10 hour batch spacing case does not reach full rank within the analysis time. When the EGI tessellation number increases considerably, there is one facet of the EGI, which is not 'observed' well, given equally space measurement batches. Therefore, a long analysis time is required to achieve full rank for the EGI Gramian. A shorter time between batches than what is tested here may have different results, but for the 1014 facet case with the time between batches of 2 to 10 hours, the EGI Gramian takes over 60 hours to become full rank. Using equally spaced measurement batches and a shorter time between batches requires more observations, thus more resources which may not actually be required if a different measurement sequence were implemented.

Next, a different approach than equally spaced batches was taken to determine a more efficient observation strategy to reach a full rank of the EGI Gramian. Figure 8 contains an unconstrained case with unequally spaced batches and two cases where constraints are imposed on the measurement times. The measurement batches are constrained by the solar depression angle and the object visibility given elevation constraints at the ground station. The night hours of the ground station are defined by a solar depression angle of 18° and the minimum elevation for object visibility is 15° at the ground station. The start times of each batch for each of the three cases are summarized in Table 1. First, the unconstrained case of Fig. 8 used results from the equally spaced analysis with $m = 13$ to space two 20 minute batches by 6 hours and then a third batch at 64 hours from the end of the second batch. This case does not consider any observation constraints based on object visibility or elevation. The first constrained case spaces two batches within the first visibility window spaced by 1.5 hours and then two more batches spaced by 1.5 hours in a visibility window after approximately 71 hours from the second batch. The second constrained batch spacing case contained one batch in each visibility window until full rank of the EGI Gramian was reached. If the object was not visible on a given night, e.g., after about 160 hours, a measurement batch did not occur.

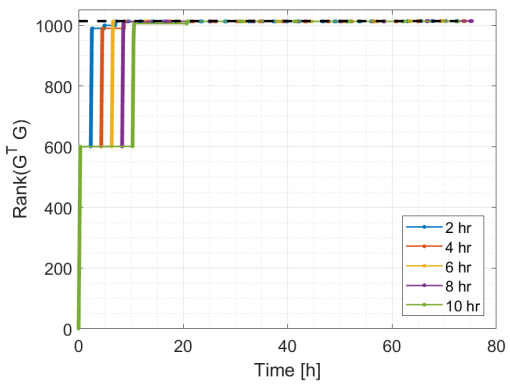

(a) Rank v. time

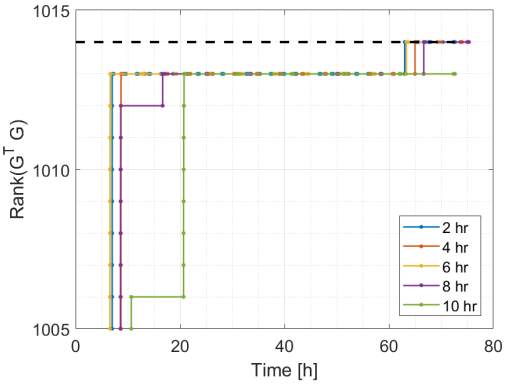

(b) Rank v. time, zoomed in to show detail

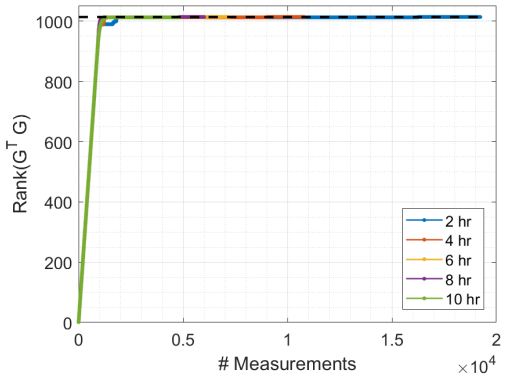

(c) Rank v. number of measurements

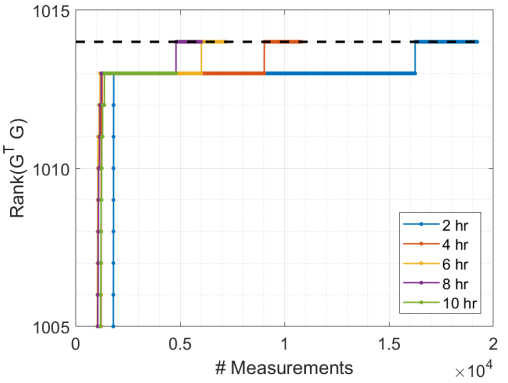

(d) Rank v. number of measurements, zoomed in to show detail

Fig. 7. Rank of the EGI Gramian for EGI tessellation of 1014 facets.

Table 1. Unconstrained and constrained batch start times, given in hours.

	Unconstrained	Constrained 1	Constrained 2
Batch 1	0.0	0.0	0.0
Batch 2	6.333	1.8333	24.0
Batch 3	70.667	73.1667	48.0
Batch 4	–	75.0	74.0
Batch 5	–	–	99.0
Batch 6	–	–	124.05
Batch 7	–	–	213.5

Figure 8 shows the rank of the EGI Gramian for the unconstrained batch spacing case and the two constrained batch spacing cases. The windows for night and object visibility are shown, with the night window given in gray and the visibility window given in green. The unconstrained case reaches full rank the fastest, which is expected as the observation times were selected using previous analysis from Fig. 7. The first constrained case reached full rank during the fourth batch of measurements, as seen in Fig. 8b. The second constrained case took significantly longer to reach full rank. This case only had one batch per visibility window, but after approximately 50 hours, the rank reached the same value as the other two cases. However, three more batches of measurements were required to reach full rank.

Figure 8c and Figure 8d show the rank of the EGI Gramian versus number of measurements. The unconstrained case required the fewest measurements to become full rank since the first constrained case had a second batch within the second night of observation. The unconstrained case was able to become full rank with only one batch of measurements

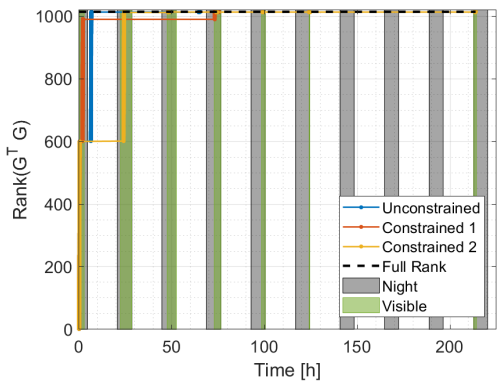

(a) Rank v. time with night and object visibility windows

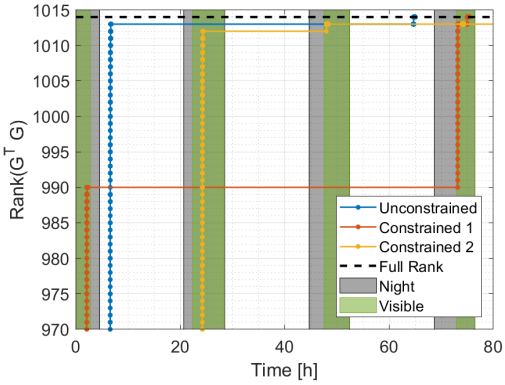

(b) Rank v. time, zoomed in to show detail

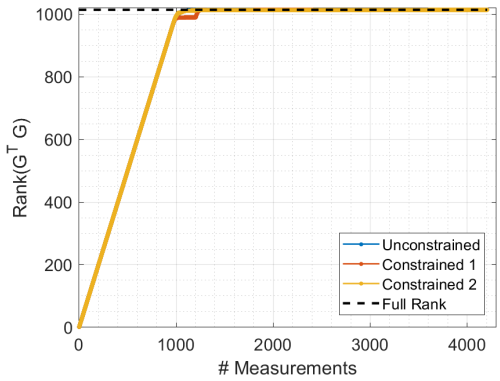

(c) Rank v. number of measurements

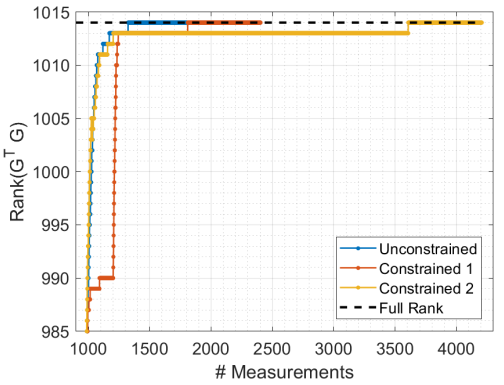

(d) Rank v. number of measurements, zoomed in to show detail

Fig. 8. Observability results for unconstrained and constrained measurement sequences. Rank of the EGI Gramian for EGI tessellation number = 13 or 1014 facets.

in the second night because the first two batches of measurements were spaced by more time; hence a greater geometry changed, and the third batch occurred in a more optimal position for the attitude and observer-object-Sun geometry.

For this EGI tessellation of 1014 facets, observing multiple batches within each visibility window is advantageous over one batch per visibility window as there are only 600 measurements per batch, and a greater geometry difference can be ensured if batches are taken twice in a visibility window. If only one batch of measurements occurs per observation window, the sampling of the geometry with the measurements may not be as diverse over two nights compared to two batches spread over one night. Even though the unconstrained case reached full rank faster than the first constrained case, selecting observation times using realistic visibility constraints to reach full rank of the EGI Gramian is possible through observability analysis. Observations do not need to be taken continuously or often during a visibility window to achieve full rank of the EGI Gramian.

4. CONCLUSIONS

The observability analysis for the shape inversion problem from un-resolved light curves has been developed. It is based on an inversion method that first estimates the extended Gaussian image followed by a geometric solution for the surface facet's adjacency relations or support. For the light curve inversion process to be successful, it is necessary for the Extended Gaussian Image (EGI) Gramian to be full rank. Observability analysis allows determining an observation schedule that is time and observation number efficient and allows for balancing other observation needs in the presence of observation constraints. The schedule differs depending on the desired shape resolution to be obtained in the inversion.

This paper focuses on the application of the methodology for observation planning for the ZIMLAT telescope, located in Switzerland, and the shape inversion for the Atlas V upper stage. The Atlas V upper stage has been assumed to be a constant single-axis spinner, and an attitude solution has been determined using three light curves. The attitude solution has been confirmed in brute force validation computations, along with a second suitable attitude solution.

Using the observability analysis, 20 minute measurement batches have been assumed with various spacings. Initially, the measurement batches were equally spaced, and the time for the EGI Gramian to reach full rank was investigated. Without constraints on the measurement times, three batches were required to reach full rank for a shape resolution of a half-angle error of 3.6, 2.7, and 1.5 degrees corresponding to a 150, 294, and 1014 facet EGI, respectively. With night time and minimum elevation constraints, four measurement batches were required to reach a full rank EGI for the 1014 facet EGI. In the constraint case, the scenario with two measurement batches per visibility window requires fewer measurements and less overall observation time, compared to the scenario with one observation batch per visibility window. The analysis shows that there is flexibility in the sensor scheduling, as observations are only required within a time region rather than a specific exact time to reach full observability.

It has been shown that observability analysis of a system can be used to select an efficient observation plan with sufficient geometric sampling for light curve shape inversion.

5. ACKNOWLEDGMENTS

This work was funded through the Department of Defense Science, Mathematics And Research for Transformation (SMART) Scholarship-for-Service Program. Thanks go to Alexander Burton for providing valuable input for this paper.

REFERENCES

[1] S. Fan and C. Frueh, "Direct Light Curve Inversion Scheme and the Influence of Measurement Noise, Journal of Astronautical Science," *Journal of Astronautical Sciences, submitted*, 2018.

[2] M. Kaasalainen, L. Lamberg, K. Lumme, and E. Bowell, "Interpretation of lightcurves of atmosphereless bodies. I - General theory and new inversion schemes," *Astronomy and Astrophysics*, Vol. 259, June 1992, pp. 318–332.

[3] D. Lynch, R. Russell, R. Rudy, D. Gutierrez, M. Turpin, K. Crawford, Y. Dotan, D. Kim, and M. Skinner, "3 - 13 μm Spectra of Geosynchronous Satellites," *The Advanced Maui Optical and Space Surveillance Technologies Conference*, 2006, p. E81.

[4] H. Cowardin, K. Abercromby, E. Barker, P. Seitzer, M. Mulrooney, and T. Schildknecht, "An Assessment of GEO Orbital Debris Photometric Properties Derived from Laboratory-Based Measurements," *Advanced Maui Optical and Space Surveillance Technologies Conference*, 2009, p. E25.

[5] R. Linares and J. L. Crassidis, "Dynamic Observability Analysis for Attitude, Angular Velocity, Shape, and Surface Parameters," *26th AAS/AIAA Space Flight Mechanics Meeting*, 2016, pp. 2016–515.

[6] T. E. Payne, S. A. Gregory, A. Dentamaro, M. Ernst, J. Hollon, A. Kruchten, A. B. Chaudhary, and P. D. Dao, "Development and Evaluation of New Methods for Estimating Albedo-area for Stable GEOs," *Advanced Maui Optical and Space Surveillance (AMOS) Technologies Conference*, 2017, p. 24.

[7] T. Schildknecht, N. Koshkin, E. Korobeinikova, S. Melikiants, L. Shakun, S. Strakhova, E. Linder, J. Silha, and M. Hager, "Photometric Monitoring of Non-resolved Space Debris and Databases of Optical Light Curves," *Advanced Maui Optical and Space Surveillance Technologies Conference*, 2015, p. 25.

[8] M. Kaasalainen, J. Torppa, and K. Muinonen, "Optimization methods for asteroid lightcurve inversion: II. The complete inverse problem," *Icarus*, Vol. 153, No. 1, 2001, pp. 37–51.

[9] V. Williams, "Location of the rotation axis of a tumbling cylindrical earth satellite by using visual observations: Part I: Theory," *Planetary and Space Science*, Vol. 27, No. 6, 1979, pp. 885–890.

[10] D. Hall, J. Africano, D. Archambeault, B. Birge, D. Witte, and P. Kervin, "Amos observations of nasa's image satellite," *The 2006 AMOS Technical Conference Proceedings*, 2006, pp. 10–14.

[11] P. Koller, "Attitude Determination of Cylindrical Rocket Bodies from Optical Light Curves," University of Bern, 2016. Bachelor Thesis.

[12] D. Gaylor and J. Anderson, "Use of hierarchical mixtures of experts to detect resident space object attitude," *Advanced Maui Optical and Space Surveillance Technologies Conference*, Vol. 1, 2014, p. 70.

[13] S. Fan, A. M. Friedman, and C. Frueh, "Satellite Shape Recovery from Light Curves with Noise," *Advanced Maui Optical and Space Surveillance Technologies Conference (AMOS)*, 2019.

[14] A. M. Friedman and C. Frueh, "Observability and Estimability Analysis of the Orbit Problem," *2019 AAS/AIAA Astrodynamics Specialist Conference*, 2019.

[15] R. Kalman, "On the General Theory of Control Systems," *IRE Transactions on Automatic Control*, Vol. 4, No. 3, 1959, pp. 110–110, 10.1109/TAC.1959.1104873.

[16] K. Ogata, *State Space Analysis of Control Systems*. Prentice-Hall, 1967.

[17] J. S. Bay, *Fundamentals of Linear State Space Systems*. McGraw-Hill Science/Engineering/Math, 1 edition ed., 1998.

[18] Z. Gajic and M. Lelic, *Modern Control Systems Engineering*. Prentice-Hall, Inc., 1997.

[19] R. Hermann and A. Krener, "Nonlinear Controllability and Observability," *IEEE Transactions on Automatic Control*, Vol. 22, No. 5, 1977, pp. 728–740, 10.1109/TAC.1977.1101601.

[20] A. M. Friedman and C. Frueh, "Determining Characteristics of Artificial Near-Earth Objects Using Observability Analysis," *Acta Astronautica*, Vol. 144, 2018, pp. 405–421, 10.1016/j.actaastro.2017.12.028.

[21] R. Zanetti and C. N. D'Souza, "Observability Analysis and Filter Design for the Orion Earth–Moon Attitude Filter," *Journal of Guidance, Control, and Dynamics*, Vol. 39, No. 2, 2016, pp. 201–213, 10.2514/1.G001217.

[22] A. Carmi and Y. Oshman, "Nonlinear Observability Analysis of Spacecraft Attitude and Angular Rate with Inertia Uncertainty," *The Journal of the Astronautical Sciences*, Vol. 57, 2013, pp. 129–148, 10.1007/BF03321498.

[23] D. Georges, "The Use of Observability and Controllability Gramians or Functions for Optimal Sensor and Actuator Location in Finite-Dimensional Systems," *, Proceedings of the 34th IEEE Conference on Decision and Control, 1995*, Vol. 4, 1995, pp. 3319–3324 vol.4, 10.1109/CDC.1995.478999.

[24] Z. Yu, P. Cui, and S. Zhu, "Observability-Based Beacon Configuration Optimization for Mars Entry Navigation," *Journal of Guidance, Control, and Dynamics*, Vol. 38, No. 4, 2015, pp. 643–650, 10.2514/1.G000014.

[25] S. C. Nardone and V. J. Aidala, "Observability Criteria for Bearings-Only Target Motion Analysis," *IEEE Transactions on Aerospace and Electronic Systems*, Vol. AES-17, No. 2, 1981, pp. 162–166, 10.1109/TAES.1981.309141.

[26] S. E. Hammel and V. J. Aidala, "Observability Requirements for Three-Dimensional Tracking via Angle Measurements," *IEEE Transactions on Aerospace and Electronic Systems*, Vol. AES-21, No. 2, 1985, pp. 200–207, 10.1109/TAES.1985.310617.

[27] E. Fogel and M. Gavish, "Nth-Order Dynamics Target Observability from Angle Measurements," *IEEE Transactions on Aerospace and Electronic Systems*, Vol. 24, No. 3, 1988, pp. 305–308, 10.1109/7.192098.

[28] J. L. Crassidis, R. Alonso, and J. L. Junkins, "Optimal Attitude and Position Determination from Line-of-Sight Measurements," 2000.

[29] D. Sun and J. L. Crassidis, "Observability Analysis of Six-Degree-of-Freedom Configuration Determination Using Vector Observations," *Journal of Guidance, Control, and Dynamics*, Vol. 25, No. 6, 2002, pp. 1149–1157, 10.2514/2.4995.

[30] A. M. Friedman, S. Fan, and C. Frueh, "Light Curve Inversion Observability Analysis," *2019 AAS/AIAA Astrodynamics Specialist Conference*, 2019.

[31] H. Minkowski, *Volumen und Oberfläche*, pp. 146–192. Springer Vienna, 1989.

[32] J. J. Little, "An Iterative Method for Reconstructing Convex Polyhedra from Extended Gaussian Images," *Proceedings of the Third AAAI Conference on Artificial Intelligence*, AAAI'83, AAAI Press, 1983, pp. 247–250.

[33] J. J. Little, "Extended Gaussian Images, Mixed Volumes, Shape Reconstruction," *Proceedings of the First Annual Symposium on Computational Geometry*, SCG '85, New York, NY, USA, ACM, 1985, pp. 15–23, 10.1145/323233.323236.

[34] J. J. Little, *Recovering shape and determining attitude from extended gaussian images*. PhD thesis, University of British Columbia, 1985, http://dx.doi.org/10.14288/1.0051804.

[35] P. Koller, "Attitude Determination of Cylindrical Rocket Bodies from Optical Light Curves," Bachelor Thesis, Astronomy Institute of the University of Bern, Under the supervision of E. Cordelli and T. Schildknecht, 2016.